AIAA JOURNAL
Vol. 30, No. 9, September 1992

Characteristic-Based, Rotated Upwind Scheme for the Euler Equations

Andrea Dadone*
Politecnico di Bari, 70125 Bari, Italy
and
Bernard Grossman†
Virginia Polytechnic Institute and State University, Blacksburg, Virginia 24061

A rotated upwind scheme is developed that calculates shock waves oblique to the grid with nearly the same resolution as shocks that are aligned with the grid. The scheme applies flux difference splitting along two orthogonal directions for each cell face, with the directions computed on the basis of pressure gradient data. Rotated extrapolations and flux limiting are used to generate second-order spatial accuracy. A filtering of the pressure gradient data allows the convergence of the rotated scheme with continuously updated upwinding angles, at a rate comparable to classical schemes. Flux evaluations based on characteristic variables and characteristic boundary conditions are discussed and implemented. The method has been tested on two simple shock reflection problems and formally second-order results capture the oblique shocks with only two to three cells in the shock transition region.

Introduction

THIS paper is concerned with the development of an upwind algorithm for multidimensional inviscid, compressible flows that accurately capture shock waves that are oblique to the grid. In general, among the numerical methods available, upwind methods have the property of appropriately mimicking physical wave-propagation phenomena associated with these flows. An upwind approach that properly accounts for the physical domain of dependence is the λ formulation,[1] but due to its inherently nonconservative framework, this formulation requires special treatment of shock waves. Conservative upwind formulations can capture shock waves, but oblique waves are often smeared over many mesh intervals, and the problem of choosing the appropriate upwind directions does not appear to be completely solved.

When one deals with one-dimensional flow problems, the choice is straightforward, since characteristic information may only be propagated in space either forward or backward. For two- or three-dimensional flow problems, the choice is more difficult, and many multidimensional schemes choose the upwinding directions to be normal to the face of the computational cell across which the fluxes are computed. Such grid-dependent schemes do not always account for the domain of dependence of each grid point. The consequences are particularly evident when shocks are computed that cross the computational mesh at an oblique angle. In such a case, the domain of dependence is violated because in the vicinity of the shock the velocity component in one of the splitting directions may be subsonic, and, accordingly, numerical information emanating downstream of the shock may reach the upstream region, causing excessive smearing of the oblique shock. Physically, such information should not propagate upstream of the shock because the flow is supersonic in the direction normal to the shock.

An early effort to develop grid-independent upwind schemes is the work of Davis,[2] who suggested upwinding angles based on possible shock-wave directions. This idea was further explored by Levy et al.[3] For each cell face a dominant direction was determined based on the flow gradient. An upwind scheme based on a local Riemann solver was used in this direction along with a central difference scheme in the direction normal to the the dominant direction. The first-order results of Levy and co-workers show very good improved resolution of oblique shock waves, with very little improvement noted for their second-order results.

A different approach was pursued by Roe[4] and was based on an approximation to a multidimensional Riemann solver. He considered local wave decompositions involving multiple acoustic waves, a shear wave and an entropy wave. Also in this category is the work of Hirsch et al.,[5,6] and the recent work of Van Ransbeeck et al.,[7] who considered a local diagonalization procedure for the Euler equations. Recently, multidimensional approaches based upon fluctuation splitting concepts, originally developed for one space dimension by Roe,[8] have been presented by Roe et al. in Refs. 9 and 10.

The preceding methods, although theoretically interesting and generally showing very promising first-order results, have not yet succeeded in producing a multidimensional upwind scheme that can accurately capture waves oblique to the grid. Indeed, in a review paper, Van Leer[11] concluded that

> The effect of a multidimensional flux function is clearly noticeable when it is used in a first-order scheme: shock and shear waves oblique to the grid are resolved as well as grid-aligned waves. When it is used in a second-order scheme, however, no further improvement is noticed, and convergence is held up. This seems to validate the use of the standard, grid-aligned second-order schemes, except possibly for hypersonic flow problems.

Following a procedure somewhat similar to to the one reported in Ref. 3, the present authors have recently suggested another first-order rotated scheme,[12] which applies flux difference splitting in two orthogonal directions for each cell face, with the directions computed on the basis of pressure gradient data. The computed results for a test problem indicated that the scheme smears oblique shock waves much less than classical first-order schemes and performs almost as well as classical second-order schemes. Moreover, a filter of the noise associated with the pressure gradient data gave the scheme a convergence rate very similar to the corresponding classical scheme,

Received March 27, 1991; revision received Jan. 7, 1992; accepted for publication Jan. 9, 1992.

*Professor, Istituto di Macchine ed Energetica. Member AIAA.
†Professor, Department of Aerospace and Ocean Engineering. Associate Fellow AIAA.

even with the use of upwinding angles which are continuously computed.

As outlined earlier, many interesting efforts have been made in the direction of exploring multidimensional flow analysis as a tool to improve the accuracy of flux-split Euler solvers. So far, significant improvements have been obtained only with first-order schemes, whereas no further advantages have been reported with second-order schemes.

The aim of the present work is to suggest a formally second-order, rotated upwind scheme that is a natural extension of our first-order scheme outlined in Ref. 12. In the rest of the paper we will first describe a standard, grid-aligned flux split procedure that will be used to test our new rotated scheme. This standard scheme will be denoted as the classical scheme throughout this paper. In conjunction with the classical scheme we will discuss the implementation of flux evaluations based on characteristic variables and the importance of characteristic boundary conditions. Then we will describe the details of our rotated scheme, including the decomposition angle computation, higher-order rotated extrapolations and limiters, and the boundary conditions in the rotated framework. The scheme will be shown to be very effective on simple shock reflection problems. It will be shown that our rotated, formally second-order scheme calculates shock waves oblique to the grid with nearly the same resolution as shocks that are aligned with the grid, with only two to three cells in the shock transition region.

The rotated scheme that we present, although influenced by the approach of Ref. 3, results in a substantially different algorithm. Some of the features of our scheme not present in Ref. 3, include the utilization of an upwind scheme in both the dominant and secondary directions, the implementation of characteristic variables and boundary conditions, a new computational stencil for interpolations, and the filtering of pressure gradient data. Our results, based on many numerical experiments, indicate substantial improvement in the resolution of oblique shock waves over standard, mesh-aligned schemes.

Classical Formulation

In this section we will briefly describe the classical flux-split formulation that we have used so that there is no ambiguity in the specific details of our comparisons of the various approaches. We adopt the procedures described by Walters, Thomas, and Van Leer in Refs. 14 and 15.

We write the vector conservation form of the two-dimensional Euler equations as

$$\frac{\partial q}{\partial t} + \frac{\partial f}{\partial x} + \frac{\partial g}{\partial y} = 0 \tag{1}$$

where the vector of conserved variables is

$$q = (\rho,\ \rho u,\ \rho v,\ \rho e_0)^T \tag{2}$$

and the flux vectors in the x and y directions are, respectively,

$$f = (\rho u,\ \rho u^2 + p,\ \rho uv,\ \rho u h_0)^T \tag{3}$$

$$g = (\rho v,\ \rho uv,\ \rho v^2 + p,\ \rho v h_0)^T \tag{4}$$

We have used the notation e_0 to refer to the total energy per unit mass (internal and kinetic) and h_0 to refer to the stagnation enthalpy, which is $h_0 \equiv e_0 + p/\rho$. The system is closed by an equation of state. For this work we consider perfect gases whereby

$$p = (\gamma - 1)\rho\left(e_0 - \frac{u^2 + v^2}{2}\right) \tag{5}$$

with γ being the ratio of specific heats.

Using a cell-centered finite-volume discretization on a quadrilateral cell sketched in Fig. 1, we obtain the semidiscrete representation as

$$A_{i,j}\frac{\partial \bar{q}_{i,j}}{\partial t} + (F\Delta s)_{i+\frac{1}{2}} - (F\Delta s)_{i-\frac{1}{2}} + (F\Delta s)_{j+\frac{1}{2}} - (F\Delta s)_{j-\frac{1}{2}} = 0 \tag{6}$$

where the $\bar{q}_{i,j}$ represents the cell area average of the vector of conserved variables q of cell i, j; $A_{i,j}$ is the area of the cell; Δs refers to the lengths of the cell edges. The vector F represents the average flux normal to the cell face given by

$$F = k_x f + k_y g = \begin{bmatrix} \rho u_\perp \\ k_x p + \rho u u_\perp \\ k_y p + \rho v u_\perp \\ \rho h_0 u_\perp \end{bmatrix} \tag{7}$$

where k_x and k_y are the direction cosines of the normal to the cell edges. The velocity component normal to the cell edge $u_\perp$ is given by

$$u_\perp = k_x u + k_y v \tag{8}$$

The velocity component tangential to the cell edge may be written as

$$u_\parallel = -k_y u + k_x v \tag{9}$$

We will utilize the well-known flux-difference splitting of Roe,[16] where the flux across each cell edge is determined by

$$F = \frac{1}{2}\left(F^- + F^+ - \sum_{i=1}^{4} e_i |\lambda_i| \alpha_i\right) \tag{10}$$

where $F^- = F(Q^-)$ and $F^+ = F(Q^+)$ refer to the flux vectors evaluated using cell-average data extrapolated to the left and right faces of the cell edge. (The left state refers to the side of the cell edge in the direction toward lower index number and the right state toward higher index number.) The wave speeds λ_i and wave strengths α_i in terms of Roe-averaged quantities are well known and were first presented in Ref. 16.

In a spatially first-order scheme, the left and right states are taken to be the cell center value to the left and right of the cell edge. For higher-order accuracy, the following extrapolation formulas[14,15] are often used. For the cell edge denoted $i - \frac{1}{2}$,

$$Q^-_{i-\frac{1}{2}} = Q_{i-1} + \tfrac{1}{4}[(1-\kappa)\nabla + (1+\kappa)\Delta]Q_{i-1}$$
$$Q^+_{i-\frac{1}{2}} = Q_i - \tfrac{1}{4}[(1-\kappa)\Delta + (1+\kappa)\nabla]Q_i \tag{11}$$

where the forward and backward differences are, respectively, $\Delta Q_i = Q_{i+1} - Q_i$ and $\nabla Q_i = Q_i - Q_{i-1}$ and the parameter κ controls the spatial accuracy; e.g., $\kappa = -1$ is second-order upwind and $\kappa = \frac{1}{3}$ is third-order upwind biased. With higher-order spatial accuracy, some form of limiting is usually required to avoid spurious oscillations in the vicinity of shock waves. In this study we will utilize the min-mod limiter. (See

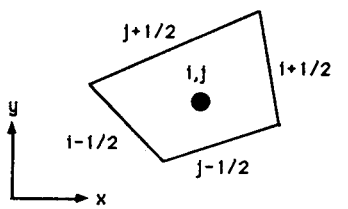

Fig. 1 Cell-centered finite volume mesh.

Sweby[17] for a discussion of limiters in general.) In Eq. (11) we replace ΔQ by $\bar{\Delta} Q$ and ∇Q by $\bar{\nabla} Q$ where

$$\bar{\Delta} Q = \text{min-mod}(\Delta Q, \beta \nabla Q)$$
$$\bar{\nabla} Q = \text{min-mod}(\nabla Q, \beta \Delta Q) \tag{12}$$

with the compression parameter $\beta = (3 - \kappa)/(1 - \kappa)$ and the min-mod function defined as min-mod$(x,y) = \text{sgn}(x) \max(0,z)$, where $z = \min[x\text{sgn}(y), y\text{sgn}(x)]$.

At this stage the quantity Q appearing in Eq. (11) must be defined. The most obvious choice is to identify it with the vector of conserved variables q as given in Eq. (2). An alternate choice, often used with high-speed flows, is to use the primitive variables

$$V = (\rho \ u \ v \ p)^T \tag{13}$$

Another choice sometimes considered for extrapolation is characteristic variables. The implementation of characteristic variables, for the appropriate one-dimensional Riemann problem at each cell edge involves utilizing the vector W:

$$W = \begin{bmatrix} (p + \rho_k a_k u_\perp)/2a_k^2 \\ (p - \rho_k a_k u_\perp)/2a_k^2 \\ \rho_k u_\parallel \\ \rho - p/a_k^2 \end{bmatrix} \tag{14}$$

where the subscript k refers to position where the wave slopes are evaluated, usually taken to be the appropriate cell centers. For example, extrapolations for the left state of cell edge $(i - \frac{1}{2})$ will involve the stencil of cell centers $(i - 2, j)$, $(i - 1, j)$ and (i, j), with k referring to $i - 1, j$. For each stencil the characteristic variables are related to the primitive variables by

$$V = R_k W \tag{15}$$

where the transformation matrix is given by

$$R_k = \begin{bmatrix} 1 & 1 & 0 & 1 \\ k_x a_k/\rho_k & -k_x a_k/\rho_k & -k_y/\rho_k & 0 \\ k_y a_k/\rho_k & -k_y a_k/\rho_k & k_x/\rho_k & 0 \\ a_k^2 & a_k^2 & 0 & 0 \end{bmatrix} \tag{16}$$

To implement the characteristic variables in the solution procedure, we should evaluate them at the appropriate stencil of cell centers and then interpolate to the appropriate cell edge using Eq. (11) and apply a limiter (12). Then the primitive variables should be evaluated from the interpolated and limited characteristic variables using Eqs. (15) and (16). This may be accomplished directly through the use of

$$V_{i-\frac{1}{2}}^- = V_{i-1} + \frac{R_{i-1}}{4}[(1 - \kappa)\bar{\nabla} + (1 + \kappa)\bar{\Delta}]W_{i-1}$$
$$V_{i-\frac{1}{2}}^+ = V_i - \frac{R_i}{4}[(1 - \kappa)\bar{\Delta} + (1 + \kappa)\bar{\nabla}]W_i \tag{17}$$

where $\bar{\Delta} W$ and $\bar{\nabla} W$ are min-mod-limited forward and backward differences.

In Ref. 13 we performed a few simple numerical calculations to evaluate the merits of the different choices of interpolation variables. We considered a shock wave that was oblique to a Cartesian grid and far from a solid boundary. The computed pressure profiles through the shock for the three choices, conserved, primitive, and characteristic, indicated some minor differences immediately downstream of the shock. The characteristic variables interpolation did appear to give the most oscillation-free results and the sharpest shock, with four mesh intervals in the shock transition zone compared to five with the other variables. In addition, for an explicit time integration, the characteristic interpolation resulted in an improved convergence rate compared to the conserved and primitive variable interpolation cases, which exhibited poor convergence often obtained using a min-mod flux limiter. Details of the pressure distributions and convergence rate may be found in Ref. 13.

Next we investigate the boundary condition at a solid surface, particularly with regard to the reflection of an oblique shock. A typical way of handling the boundary condition at a wall, where the only quantity required for an inviscid calculation is the surface pressure, generally involves a simple extrapolation. Usually, values of pressure on the surface are taken to be the value at the nearest cell center. This can result in a possible inconsistency, since, even in the limit of vanishing cell size, an oblique shock may lie between the cell center and the surface. Alternatively, characteristic boundary conditions can be employed, which, in the spirit of the present quasi-one-dimensional interpolation and first-order spatial accuracy, enforce the constancy of either the first or second component of the vector W in Eq. (14). Taking into account that the velocity normal to the surface must be zero, we obtain

$$p_w = \begin{cases} p_1 - \rho_1 a_1 u_\perp, & \text{lower wall} \\ p_1 + \rho_1 a_1 u_\perp, & \text{upper wall} \end{cases} \tag{18}$$

where the subscripts w and 1 refer to the wall and the nearest cell center, respectively.

To compare the characteristic boundary condition with the extrapolated pressure condition, we performed calculations on a simple test problem of an oblique shock reflecting from a flat plate. The incident shock angle was chosen to be -29 deg and the freestream Mach number was $M_\infty = 2.9$. We used a uniform 61×33 grid on a rectangular region of length 2.75 and height of 1. This is the identical test problem used in Ref. 6, and will be used later in this paper to evaluate the rotated algorithm.

The pressure distribution along the wall is indicated in Fig. 2, which compares calculations with the characteristic boundary condition to the extrapolated pressure condition and the exact result. Again, differences appear in the behavior immediately downstream of the shock, with the characteristic boundary conditions giving the best results. Based on the results presented in this section, we will adopt characteristic interpolation (17) and characteristic boundary conditions (18) in our reference or classical scheme. This reference code will be used in the following to evaluate the effectiveness of our rotated formulation.

Rotated Formulation

It is well established that computations of shock waves that are oblique to the mesh are more highly smeared than those

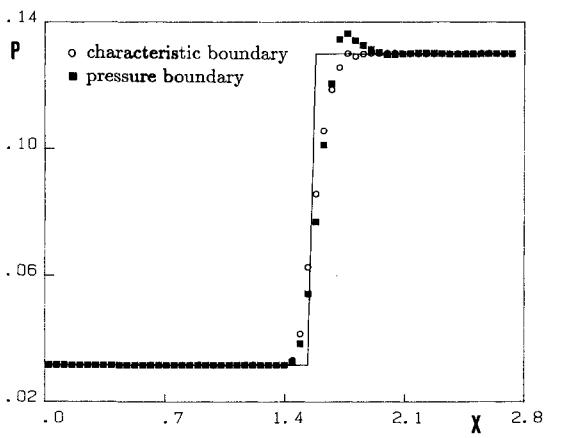

Fig. 2 Surface pressure distribution for shock reflection problem.

that are aligned with one of the mesh directions. Indeed, calculations using second-order upwind algorithms generally result in a shock wave spread over two to three cells in the aligned case, but as many as four to eight cells for oblique waves, with the situation becoming even more severe in the vicinity of a solid surface. This situation is confirmed by our classical calculations shown in Fig. 2 and in Ref. 13. This shock spreading would be reduced if a new mesh oriented orthogonally to the shock were employed. This forms the basis of our rotated formulation, which attempts to reproduce an orthogonal shock situation without actually changing the mesh. We proceed by examining pressure gradient data to determine a privileged direction that coincides with the direction normal to an oblique shock. Each cell edge is then decomposed into two surfaces, one orthogonal and the other parallel to this particular direction. The fluxes through each of these cell-edge components are evaluated by appropriate rotated interpolation, in an attempt to mimic an orthogonal shock situation.

The flux across a generic cell edge, $F\Delta s$ in Eq. (6), may be expanded as

$$F\Delta s = F_{\perp}\Delta s \cos\alpha' + F_{\parallel}\Delta s \sin|\alpha'| \tag{19}$$

where α' is the angle of the privileged or upwinding direction with respect to the normal to the considered cell edge, $F_{\perp}$ and $F_{\parallel}$ are the flux components respectively along and normal to this direction, respectively, and $\Delta s \cos\alpha'$ and $\Delta s \sin|\alpha'|$ are the projected cell-edge lengths.

Note that, if $F_{\perp}$ and $F_{\parallel}$ were evaluated using the same cell centers used to interpolate F in a nonrotated frame, no basic change from the usual oblique shock results would be expected. However, by interpolating $F_{\perp}$ and $F_{\parallel}$ from cell centers close to normal to their respective cell-edge components, a situation closer to a normal shock calculation would be simulated.

An alternate interpretation of the need for this type of approach can be obtained by examining the wave propagation of a shock oblique to the mesh as discussed in the Introduction. With the cell-edge decomposition, the velocity components orthogonal to the shock in the upstream region remain supersonic, avoiding the unphysical numerical propagation. The rotated interpolations will also tend to reduce unphysical propagations in the direction parallel to the shock. Before we proceed with the rotated interpolation formulas, we will first address the decomposition-angle computation.

Decomposition-Angle Computation

The local pressure = gradient angle is computed at each cell edge, utilizing the procedures of Ref. 3. For cell edge $(i - \frac{1}{2})$ we define

$$\begin{aligned} p_w &= \tfrac{1}{4}(p_{i-1,j-1} + 2p_{i-1,j} + p_{i-1,j+1}) \\ p_e &= \tfrac{1}{4}(p_{i,j-1} + 2p_{i,j} + p_{i,j+1}) \\ p_n &= \tfrac{1}{2}(p_{i-1,j+1} + P_{i,j+1}) \\ p_s &= \tfrac{1}{2}(p_{i-1,j-1} + p_{i,j-1}) \end{aligned} \tag{20}$$

The computational derivatives in the physical plane become

$$\begin{aligned} \frac{\partial p}{\partial x} &= \frac{(p_e - p_w)}{\Delta\xi}\frac{\partial \xi}{\partial x} + \frac{(p_n - p_s)}{2\Delta\eta}\frac{\partial \eta}{\partial x} \\ \frac{\partial p}{\partial y} &= \frac{(p_e - p_w)}{\Delta\xi}\frac{\partial \xi}{\partial y} + \frac{(p_n - p_s)}{2\Delta\eta}\frac{\partial \eta}{\partial y} \end{aligned} \tag{21}$$

where $\partial\xi/\partial x/\Delta\xi$, $\partial\xi/\partial y/\Delta\xi$, $\partial\eta/\partial x/\Delta\eta$, and $\partial\eta/\partial y/\Delta\eta$ are the metric derivatives. The magnitude of the pressure gradient follows from

$$|\nabla p| = \sqrt{\left(\frac{\partial p}{\partial x}\right)^2 + \left(\frac{\partial p}{\partial y}\right)^2} \tag{22}$$

and the corresponding angle measured with respect to the x axis is

$$\theta = \tan^{-1}\left(\frac{\partial p/\partial y}{\partial p/\partial x}\right) \tag{23}$$

The use of the formula (23) gives a sufficiently smooth variation from cell to cell when the shock is smeared, such as in the first-order case. For higher-order spatial accuracy we have found it necessary to average this angle with the surrounding cell-edge values. In addition, above formula (23) gives meaningless results in regions where the gradients are nearly zero. We have incorporated a filtering whereby we examine the ratio of the local value of the pressure gradient magnitude to the maximum value of this quantity everywhere in the field. Where this ratio is >0.20, we use the angle computed from formula (23); where the ratio is <0.10 we set the angle to zero. For values between 0.10 and 0.20, we use a linear interpolation between the angle in formula (23) and zero. The aforementioned procedures for smoothing and filtering the pressure gradient data differ from Ref. 3 and are seen to be valid for Cartesian and nearly Cartesian grids.

At this stage we may observe that, in the determination of the upwinding angle, the sense of the direction is unimportant. Hence, it will only be necessary to determine the angle between the pressure gradient direction and the normal to the cell edge to within ± 90 deg. Furthermore, we will be decomposing the fluxes into two components: one along the pressure-gradient direction and one normal to it. One of the directions will always be within ± 45 deg of the normal to the cell edge. Since we will be solving a Riemann problem in each direction, it is not necessary to identify the directions as normal or tangential to the pressure-gradient direction. It greatly simplifies our topology if we introduce an angle α, which we call the cell-edge decomposition angle and is the angle between the cell-edge normal and either the pressure gradient angle or its normal, such that $-45 \text{ deg} \le \alpha \le 45$ deg. In practice, we take α as the angle between the line connecting two cell centers traversing the considered cell edge and the pressure gradient angle or its normal. We will then decompose the fluxes into two components, F_1 and F_2, where F_1 is the component along α and F_2 is the component normal to α. We see that $F_1 = F_{\perp}$ and $F_2 = F_{\parallel}$ in Eq. (19) if $-45 \text{ deg} \le \alpha' \le 45$ deg. Otherwise their roles are reversed. The introduction of the cell-edge decomposition angle greatly simplifies the interpolation technique in the rotated frame, which will be described next.

Rotated Interpolations

First we examine rotated interpolations resulting in a first-order spatially accurate scheme. Consider an $(i - \frac{1}{2})$ cell edge and a negative cell-edge decomposition angle α with normal flux components F_1 and F_2 as indicated in the sketch in Fig. 3. We evaluate these fluxes from their left and right states as $F_1 = F_1(Q_1^-, Q_1^+)$ and $F_2 = F_2(Q_2^-, Q_2^+)$. Then for a first-order spatially accurate scheme, we take

$$\begin{aligned} (Q_1^-)_{i-\frac{1}{2}} &= Q_{i-1,j} \\ (Q_1^+)_{i-\frac{1}{2}} &= Q_{i,j} \end{aligned} \tag{24}$$

and

$$\begin{aligned} (Q_2^-)_{i-\frac{1}{2}} &= Q_{i-1,j\mp 1} \\ (Q_2^+)_{i-\frac{1}{2}} &= Q_{i,j\pm 1} \end{aligned} \tag{25}$$

where the upper sign in Eq. (25) is used when $\alpha<0$ and the lower sign for $\alpha>0$. We may note that for $\alpha = 0$, the flux F_1

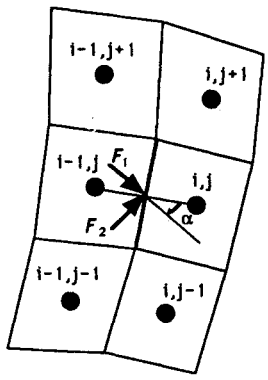

Fig. 3 Rotated frame.

corresponds to the flux normal to the cell edge, and the classical scheme is retained. Otherwise the first-order treatment of the states $Q_1^{\pm}$ are evaluated in the classical fashion, whereas the states $Q_2^{\pm}$ are rotated to the nearest cell centers.

For the $(j - \frac{1}{2})$ cell edge, a similar decomposition applies. Recalling our definition of the decomposition angle α, now measured with respect to the normal to the $(j - \frac{1}{2})$ cell edge, we have

$$(Q_1^-)_{j-\frac{1}{2}} = Q_{i,j-1}$$
$$(Q_1^+)_{j-\frac{1}{2}} = Q_{i,j} \tag{26}$$

and

$$(Q_2^-)_{j-\frac{1}{2}} = Q_{i\pm 1,j-1}$$
$$(Q_2^+)_{j-\frac{1}{2}} = Q_{i\mp 1,j} \tag{27}$$

The convenience of introducing the decomposition angle should be evident. We may note the symmetry between the $(i - \frac{1}{2})$ cell edge and the $(j - \frac{1}{2})$ edge through Eqs. (24-27). The other cell edges may be evaluated accordingly.

A higher-order space-accurate scheme can be obtained by blending the rotated first-order scheme with a traditional, higher-order mesh-oriented interpolation. In this approach the advantages of the rotated scheme will be preserved near a shock wave, where the flux limiters will reduce the accuracy. The rotated scheme will maintain the appropriate domain of dependence of the scheme near oblique shocks. Away from shocks, the traditional higher-order scheme is used. We accomplish this interpolation by using an estimated value of the right and left cell-edge component value obtained by the usual mesh oriented interpolation as in Eq. (11) or with characteristic variables, [Eq. (17)]. Backward and forward increments are developed with these values and the first-order rotated values.

For example, again consider the $(i - \frac{1}{2})$ cell edge, which is sketched with a negative decomposition angle α in Fig. 3. In a fashion similar to the first-order treatment, we will determine the higher-order evaluation of the states $Q_1^{\pm}$ in the classical fashion from Eq. (11). The procedure for the states $Q_2^{\pm}$ is more complicated, as indicated in the following procedure. For the left state of Q_2^-, we obtain

$$(Q_2^-)_{i-\frac{1}{2}} = Q_{i-1,j\mp 1} + \tfrac{1}{4}[(1-\kappa)\tilde{\nabla} + (1+\kappa)\tilde{\Delta}]Q_{i-1}^- \tag{28}$$

where the modified forward and backward differences, $\tilde{\Delta}Q_{i-1}^-$ and $\tilde{\nabla}Q_{i-1}^-$, are taken along a line between the first-order cell centers $(i-1, j \mp 1)$ and $(i, j \pm 1)$ as

$$\tilde{\nabla}Q_{i-1}^- = 2(Q_{i-\frac{1}{2}}^- - Q_{i-1,j\mp 1})$$
$$\tilde{\Delta}Q_{i-1}^- = (Q_{i,j\pm 1} - Q_{i-1,j\mp 1}) \tag{29}$$

The term $Q_{i-\frac{1}{2}}^-$ is estimated to second order by a standard mesh-oriented interpolation, [Eq. (11)]. Again, the upper sign is used for negative angle α and the lower sign for positive α. Similar formulas are used for the right state, whereby

$$(Q_2^+)_{i-\frac{1}{2}} = Q_{i,j\pm 1} - \tfrac{1}{4}[(1-\kappa)\tilde{\Delta} + (1+\kappa)\tilde{\nabla}]Q_{i-1}^+ \tag{30}$$

with

$$\tilde{\nabla}Q_{i-1}^+ = (Q_{i,j\pm 1} - Q_{i-1,j\mp 1})$$
$$\tilde{\Delta}Q_{i-1}^+ = 2(Q_{i,j\pm 1} - Q_{i-\frac{1}{2}}^+) \tag{31}$$

and again $Q_{i-\frac{1}{2}}^+$ is evaluated from Eq. (11).

We may extend Eqs. (28-31) to the $j - \frac{1}{2}$ cell edge by

$$(Q_2^-)_{j-\frac{1}{2}} = Q_{i\pm 1,j-1} + \tfrac{1}{4}[(1-\kappa)\tilde{\nabla} + (1+\kappa)\tilde{\Delta}]Q_{j-1}^- \tag{32}$$
$$(Q_2^+)_{j-\frac{1}{2}} = Q_{i\mp 1,j} - \tfrac{1}{4}[(1-\kappa)\tilde{\Delta} + (1+\kappa)\tilde{\nabla}]Q_{j-1}^+$$

with

$$\tilde{\nabla}Q_{j-1}^- = 2(Q_{j-\frac{1}{2}}^- - Q_{i\pm 1,j-1})$$
$$\tilde{\Delta}Q_{j-1}^- = (Q_{i\mp 1,j} - Q_{i\pm 1,j-1})$$
$$\tilde{\nabla}Q_{j-1}^+ = (Q_{i\mp 1,j} - Q_{i\pm 1,j-1}) \tag{33}$$
$$\tilde{\Delta}Q_{j-1}^+ = 2(Q_{i\mp 1,j} - Q_{j-\frac{1}{2}}^+)$$

where $Q_{j-\frac{1}{2}}^{\pm}$ is evaluated from Eq. (11).

A flux limiter may also be introduced at this stage. On the basis of our numerical experiments, we have found that the Chakravarthy-Osher (C-O) limiter described in Ref. 17 performed best for the rotated formulation. The results using this limiter were very slightly better than those using the min-mod limiter, discussed in connection with the classical formulation. The only noticeable effect was with the first mesh upstream of the shock, resulting in a very slightly steeper shock with the C-O limiter. We note that using this limiter with the classical formulation had an opposite result. In keeping with our objective of comparing the best possible classical formulation with our rotated formulation, we utilize the min-mod limiter with the classical computations and the C-O limiter with the rotated calculations. However, the differences are quite minor and do not affect any of the conclusions.

The C-O limiter may be defined as

$$\mathcal{L}(x, y) = x \max[0, \min(y/x, \beta)] \tag{34}$$

where in our application we set the free parameter $\beta = 2$. We introduce this limiter by modifying the differences $\tilde{\Delta}Q^{\pm}$ and $\tilde{\nabla}Q^{\pm}$ in Eqs. (28), (30), and (32) as

$$\tilde{\Delta}Q^{\pm} = \mathcal{L}(\tilde{\Delta}Q^{\pm}, \tilde{\nabla}Q^{\pm})$$
$$\tilde{\nabla}Q^{\pm} = \mathcal{L}(\tilde{\nabla}Q^{\pm}, \tilde{\Delta}Q^{\pm}) \tag{35}$$

Furthermore, the higher-order interpolations in Eqs. (28), (30), and (32) may be modified to interpolate characteristic variables in a fashion very similar to Eq. (17). The formulas become

$$(V_2^-)_{i-\frac{1}{2}} = V_{i-1,j\mp 1} + \frac{R_{i-1,j\mp 1}}{4}[(1-\kappa)\tilde{\nabla} + (1+\kappa)\tilde{\Delta}]W_{i-1}^-$$
$$(V_2^+)_{i-\frac{1}{2}} = V_{i,j\pm 1} - \frac{R_{i,j\pm 1}}{4}[(1-\kappa)\tilde{\Delta} + (1+\kappa)\tilde{\nabla}]W_{i-1}^+ \tag{36}$$
$$(V_2^-)_{j-\frac{1}{2}} = V_{i\pm 1,j-1} + \frac{R_{i\pm 1,j-1}}{4}[(1-\kappa)\tilde{\nabla} + (1+\kappa)\tilde{\Delta}]W_{j-1}^-$$
$$(V_2^+)_{j-\frac{1}{2}} = V_{i\mp 1,j} - \frac{R_{i\mp 1,j}}{4}[(1-\kappa)\tilde{\Delta} + (1+\kappa)\tilde{\nabla}]W_{j-1}^+$$

where $\bar{\Delta}W$ and $\bar{\nabla}W$ are the C-O limited evaluation [see Eq. (35)] of the differences given in Eqs. (29), (31), and (33) with the variables Q taken to be the characteristic variables W.

Rotated Boundary Conditions

The rotated formulation requires special treatment of the surface boundary conditions in the vicinity of a shock reflection. Consider the situation sketched in Fig. 4. The incident shock AB reflects on the wall DE generating a reflected shock BC. Assume that the cell centers $(i,1)$ and $(i+1,1)$ are separated from the corresponding wall points $(i,0)$ and $(i+1,0)$ by the incident and reflected shocks, respectively. The computation of the boundary values at $(i,0)$ on the basis of information at $(i,1)$ is not physical, since it would imply that numerical data emanating downstream of the incident shock would reach the upstream region. On the other hand, the computation of the wall point $(i+1,0)$ on the basis of information from $(i+1,1)$ can be physically acceptable. When dealing with a classical mesh-oriented calculation, no information about the shock slopes is available, so that the two cases cannot be discriminated. One may expect to occasionally encounter some oscillations near shock reflections using the classical formulation, even with characteristic boundary conditions.

For the rotated framework discussed here, since we do have shock slope information, we can attempt to resolve this situation. We have adopted a very simple procedure where the values of the pressure at upstream cell centers have been used to evaluate the conditions at wall points located close to incident shocks, whereas characteristic boundary conditions are used at wall points close to reflected shocks. In Fig. 4, the pressure at $(i-1,1)$ is used to determine the pressure at the wall $(i,0)$ and conditions at $(i+1,1)$ are used in the characteristic boundary condition (18) to determine the surface pressure at $(i+1,0)$. This relatively simple approach will be seen to produce acceptable results, although small oscillations sometimes appear, as will be discussed in the next section. More complicated procedures based on the multidimensional method of characteristics could have been devised to fully account for the appropriate domain of dependence.

Results

We have performed a few very simple test calculations to validate the rotated frame formulation on problems with oblique shocks. The first case considered was an isolated oblique shock. The problem involved an incoming shock penetrating a $M_\infty = 2.9$ freestream, making an angle of -29 deg to the horizontal. A 33×33 grid was used on a rectangular region of length 1.5 and height of 1. The first-order spatially accurate results were presented in Ref. 13, where the computed results for the rotated formulation and the classical mesh-oriented formulation were compared to the exact solution. We found that the number of points involved in the shock transition was reduced by a factor of 2 with the rotated formulation. We also define a quantity called the pressure-slope error as the difference between the slope of the pressure distribution in the shock transition region and the exact (normal) value. For the first-order case the rotated formulation reduced the pressure-slope error by a factor of 4.

In order to develop the higher-order formulation for the rotated framework, many variations of the extrapolation procedure and limiter choice were tested. The best overall performance was obtained from the choice outlined in Eqs. (28–36). The second-order space-accurate solution along a horizontal line through the shock is presented here in Fig. 5. We see that the rotated formulation develops a much steeper shock, compared to the second-order-accurate classical formulation. From the figure we see that there are only two to three cells in the shock transition region, approximately half of the number in the classical result.

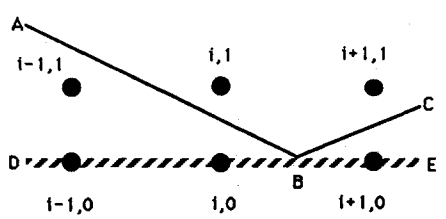

Fig. 4 Boundary condition near a shock reflection.

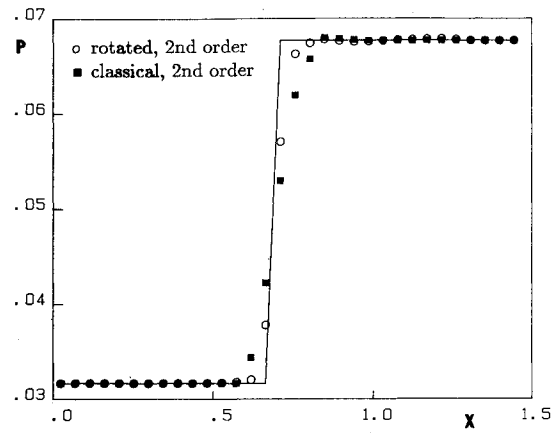

Fig. 5 Pressure distribution through an oblique shock: second-order result.

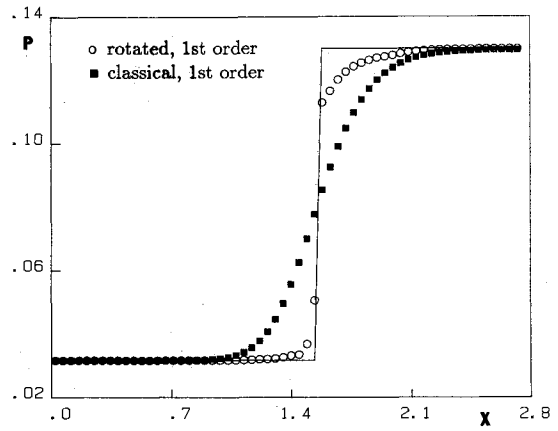

Fig. 6 Surface pressure distribution for shock reflection problem: first-order result.

Next we consider the $M_\infty = 2.9$ shock incident at -29 deg reflecting off a solid boundary. We compute the solution with the same 61×33 grid used in the calculations presented in Fig. 2. The first-order spatially accurate results will be described first. The surface pressure distribution is plotted for the classical, rotated, and exact solutions in Fig. 6. We again see that the rotated formulation reduces the number of mesh points in the shock transition region by a factor of 2 and that the pressure-slope error is reduced by a factor of at least 4. However, the results indicate that downstream portion of the shock transition is more smeared than would be expected for the rotated formulation, possibly indicating a need for an improved boundary procedure. More details of this calculation are given in Ref. 13, where a comparison of the isopycnics indicated that the rotated formulation produced a much sharper reflected shock than the classical mesh-oriented result. Examination of the contours in the classical case indicated some small oscillations in the direction normal to the plate, which are probably due to the improper application of the characteristic boundary condition very near the shock intersection, as discussed previously. This situation is somewhat improved with the application of the boundary conditions in the rotated framework. Also presented in Ref. 13 are plots of

the density distribution along a vertical line at the outlet of the domain, where the sharpness of the shock returned away from the wall. For this problem the convergence rate with the rotated formulation was not affected by the continuously updated upwinding angles.

Next we considered second-order space-accurate solutions for the shock reflection problem. The density contours for the classical case are shown in Fig. 7a, and for the rotated case is shown in Fig. 7b. The surface pressure distributions are presented in Fig. 8. These results confirm the conclusions drawn for the first-order case: The rotated formulation can produce shocks with reduced numbers of cells involved in the shock transition and greatly reduced pressure-slope errors. We also observe that along the wall a small oscillation occurs just downstream of the shock. This wiggle is probably due to the boundary condition discussed previously. Otherwise the shock transition with the rotated formulation is very abrupt, with nearly a three-cell transition, which would be expected if the shock were perfectly aligned with the grid. The crispness of the rotated calculation of the reflected shock away from the wall is observed in our results. Further results for this test problem appear in Ref. 13, including density distributions through the shock in a direction normal to the wall, plots of the computed shock angles, and convergence rates.

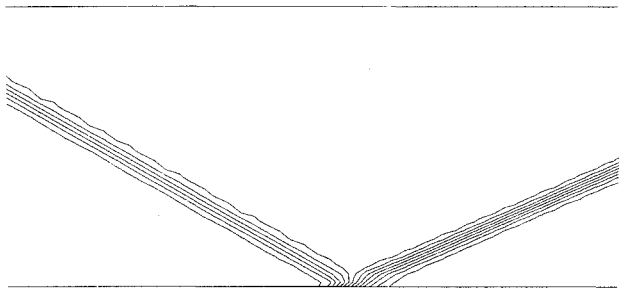

Fig. 7a Density contours for shock reflection problem: second-order classical result.

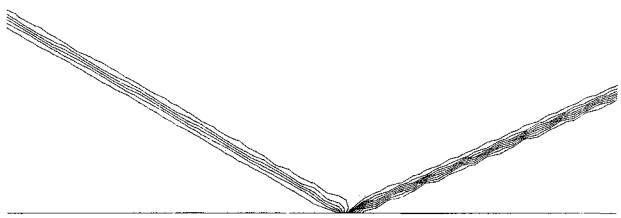

Fig. 7b Density contours for shock reflection problem: second-order rotated result.

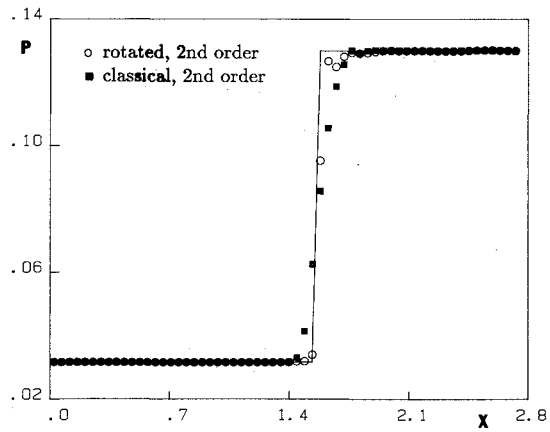

Fig. 8 Surface pressure distribution for shock reflection problem: second-order result.

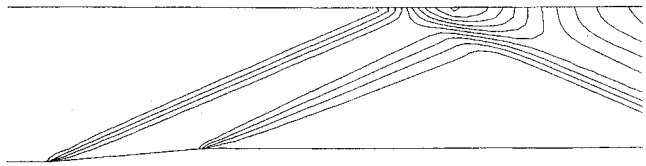

Fig. 9a Density contours for supersonic channel problem: second-order classical result.

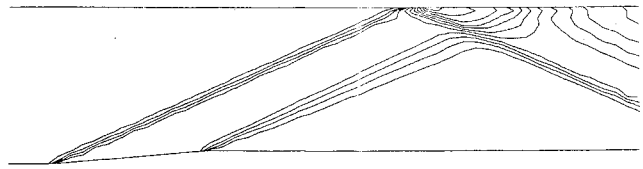

Fig. 9b Density contours for supersonic channel problem: second-order rotated result.

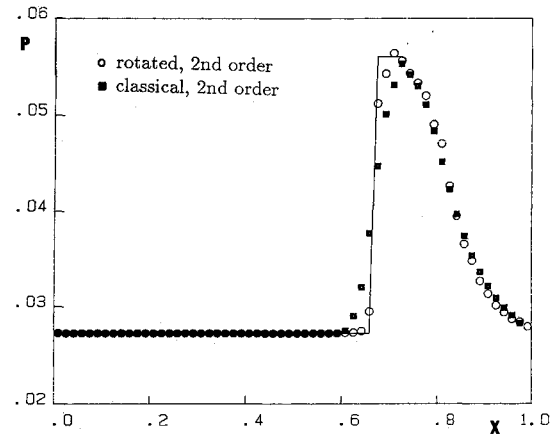

Fig. 10 Upper-wall pressure distribution for supersonic channel problem: second-order result.

Another test case is the $M_\infty = 3.0$ flow through a two-dimensional channel. The channel entrance is a 5-deg compression ramp followed by an expansion corner parallel to the entrance flow. The scaled length of the channel is 1.0 with an entrance height of 0.2 and the compression ramp located between $0.2 \leq x \leq 0.4$. The flow in the channel includes a shock emanating from the compression corner and reflecting from the upper wall, and an expansion fan that interacts with the reflected shock and finally reflects off the upper wall. A 61×21 grid was used to compute second-order space-accurate results using both the classical and rotated framework. The computed density contours for the classical and rotated approaches are presented in Figs. 9a and 9b, respectively. The contours reaffirm the findings that the rotated formulation gives improved resolution for both the incident and reflected shocks. An examination of Fig. 9b indicates the presence of a mild oscillation in the direction normal to the wall, which is probably due to the boundary conditions discussed previously. The pressure distribution on the upper wall is plotted in Fig. 10. We see the improved resolution on the upper wall of the shock reflection using the rotated formulation.

Conclusions

The objective of this work was to develop a rotated upwind scheme that calculates shocks oblique to a grid with the same resolution as shocks that are aligned with the grid. We feel that we have nearly attained this goal. Our second-order results capture shocks with only two to three cells in the shock transition region, which is a considerable improvement over existing methods. The scheme applies flux difference splitting along two orthogonal directions for each cell face, with the

directions computed on the basis of pressure gradient data. Rotated extrapolations and flux limiting are used to generate second-order spatial accuracy. A filtering of the pressure-gradient data allows the convergence of the rotated scheme with continuously updated upwinding angles at a rate comparable to classical schemes. We have discussed the implementation of characteristic variable extrapolations and the efficacy of characteristic boundary conditions.

A number of areas remain that require further study. We have examined the method only for a class of simple shock reflections. To validate our approach we must consider more difficult problems over general geometries. Also, we feel that an improved surface boundary condition based on the method of characteristics for multidimensional flows would be very desirable. The issue of the best limiter to use for these flows could certainly stand further scrutiny. Furthermore, if this approach is to be of practical use, the method must be extended to three space dimensions and ways of improving the computational efficiency should be sought. The rotated formulation requires the solution of two Riemann problems at each cell face, instead of the usual 1, along with the minor overhead of the decomposition angle computation. However, we feel that classes of problems exist that require greatly improved shock resolution even at the expense of some computational efficiency.

Acknowledgments

The research of the first author was supported by the Italian agencies Consiglio Nazionale della Richerche and Ministero dell'Università e della Ricerca Scientifica e Tecnologica. The second author acknowledges the assistance of the National Science Foundation under the U.S.-Italy Cooperative Science Program, Grant INT-8814895 and the support of CNR while he was in Bari in the spring of 1990.

References

[1]Moretti, G., "The λ-Scheme," *Computers and Fluids,* Vol. 7, 1979, pp. 191–205.

[2]Davis, S. F., "A Rotationally-Biased Upwind Difference Scheme for the Euler Equations," *Journal of Computational Physics,* Vol. 56, 1984, pp. 65–92.

[3]Levy, D. W., Powell, K. G., and Van Leer, B., "An Implementation of a Grid-Independent Upwind Scheme for the Euler Equations," AIAA Paper 89-1931-CP, June 1989.

[4]Roe, P. L., "Discrete Models for the Numerical Analysis of Time-Dependent Multidimensional Gas Dynamics," *Journal of Computational Physics,* Vol. 63, 1986, pp. 458–476.

[5]Hirsch, C., Lacor, C., and Deconinck, H., "Convection Algorithms Based on a Diagonalization Procedure for the Multidimensional Euler Equations," AIAA Paper 87-1163-CP, June 1987.

[6]Hirsch, C., and Lacor, C., "Upwind Algorithms Based on a Diagonalization of the Multidimensional Euler Equations," AIAA Paper 89-1958, June 1989.

[7]Van Ransbeeck, P., Lacor, C., and Hirsch, C., "A Multidimensional Cell-Centered Upwind Algorithm Based on a Diagonalization of the Euler Equations," *Proceedings of the Twelfth International Conference on Numerical Methods in Fluid Mechanics,* Berlin, July 1990, Lecture Notes in Physics, Vol. 371, Springer-Verlag, pp. 238–242.

[8]Roe, P. L., "Fluctuations and Signals, a Framework for Numerical Evolution Problems," *Numerical Methods for Fluid Dynamics,* edited by K. W. Morton M. J. Baines, Academic, New York, 1982, pp. 219–257.

[9]Roe, P. L., Deconinck, H., and Struijs, R., "Recent Progress in Multidimensional Upwinding," *Proceedings of the Twelfth International Conference on Numerical Methods in Fluid Mechanics,* Berlin, July 1990, Lecture Notes in Physics, Vol. 371, Springer-Verlag, pp. 273–277.

[10]Struijs, R., Deconinck, H., and De Palma, P., "Multidimensional Upwind Schemes Using Fluctuation Splitting and Different Wave Models for the Euler Equations," *Proceedings of the Twelfth International Conference on Numerical Methods in Fluid Mechanics,* Berlin, July 1990, Lecture Notes in Physics, Vol. 371, Springer-Verlag, pp. 352–354.

[11]Van Leer, B., "Advancing the Accuracy and Efficiency of Explicit Euler Solvers," AIAA Paper 90-0012, Jan. 1990.

[12]Dadone, A., and Grossman, B., "A Domain of Dependence Upwind Scheme for the Euler Equations," *Proceedings of the Twelfth International Conference on Numerical Methods in Fluid Mechanics,* Berlin, July 1990, Lecture Notes in Physics, Vol. 371, Springer-Verlag, pp. 379–380.

[13]Dadone, A., and Grossman, B., "A Rotated Upwind Scheme for the Euler Equations," AIAA Paper 91-0635, Jan. 1991.

[14]Walters, R. W., and Thomas, J .L., "Advances in Upwind Relaxation Methods," *State-of-the-Art Surveys of Computational Mechanics,* edited by A. K. Noor, American Society of Mechanical Engineers, New York, 1988, Chap. 4.

[15]Thomas, J. L., Van Leer, B., and Walters, R. W., "Implicit Flux-Split Schemes for the Euler Equations," AIAA Paper 85-1680, July 1985.

[16]Roe, P. L., "Approximate Riemann Solvers, Parameter Vectors and Difference Schemes," *Journal of Computational Physics,* Vol. 43, 1981, pp. 357–372.

[17]Sweby, P. K., "High Resolution Schemes Using Flux Limiters for Hyperbolic Conservation Laws," *Journal of Numerical Analysis,* Vol. 21, No.5, 1984, pp. 995–1011.